Journal of Medical Systems (2019) 43: 34
https://doi.org/10.1007/s10916-018-1148-6

MOBILE & WIRELESS HEALTH

Non-Linear Filtering Technique Used for Testing the Human Lumbar Spine FEA Model

E. Punarselvam [1] · P. Suresh [2]

Received: 5 November 2018 / Accepted: 19 December 2018 / Published online: 6 January 2019

Abstract

In this paper, the objective is to generate a mesh model of a spine that simulates numerically the biomedical properties of two vertebrae (L4 and L5) of human spine and an inter vertebrae disc using Finite Element Analysis (FEA) technique. Here, different types of non-linear filters and different edge detection techniques are used to segment the edges and the results are compared. The result shows that median filter obtains improved segmented output results in terms of edge length density, average magnitude, final threshold, initial position, and fine-tuned image. The behaviour of spine FEA model is analysed in terms of various parameters like equivalent elastic strain, total deformation, maximum principal elastic strain, minimum principal elastic strain, shear elastic strain, normal elastic strain, and minimum and maximum principal stress, equivalent stress, shear stress and normal stress. These parameters are used to analyse the human spine model under different conditions and different angles using ANSYS simulation tool. Further, MATLAB is carried out to implement various filters and edge detectors on proposed spine model.

Keywords Filters · Edge detection · MRI · Finite element analysis

Introduction

In this era, lower back pain is considered as a serious disease and this is referred as Lumbar Degenerative Disc Disease (LDDD), which is caused due to overloading and aging. Pathological conditions that affects the lumbar spine includes osteoporosis, low back pain (LBP), herniation or spondylolisthesis has acute problems [1]. The diagnosis of such ailments and pathologies treatment require quantitative analysis on MRI spinal images of multiple anatomic structures in multiple anatomic planes from multiple imaging modalities [2].

This poses a challenge in computer and manual processing methods.

- Manual processing methods is infeasible for MRI images due to inefficiency, tediousness and inconsistency [3].
- Computer processing methods achieves initial success on efficient processing of spinal images [4, 5].

However, it is unable to handle images, since the image segmentation leads to extreme challenging that involves: 1) Different structure appearance on disc and vertebra; 2) Different intensity profiles of MRI; 3) Different shapes in different plane. The segmentation of image plays a major role in image processing. It is used to identify the edges of image objects with multiple contour pixels set. The pixels represent the object information and it is classified into two types, namely edge and region based segmentation. The proposed study uses edge based segmentation to extract the edges [6]. The filtering operation in an image is used to deblur digital images. It is used to smoothen the images using appropriate masking function [7]. The filters are used to detach the noises from an image and it enhances the image. For the pre-processing operation, the boundary is discovered in MRI images using various edge detection algorithm. These images are further sent to other processing stages for the creation of 3D meshes and its analysis [8]. Finite element method (FEM) is a common method or tool used in numerical simulation to analyse the thermodynamics or mechanics of image structure. The proposed

This article is part of the Topical Collection on *Mobile & Wireless Health*

✉ E. Punarselvam
punarselvam83@gmail.com

[1] Department of Information Technology, Muthayammal Engineering College, Rasipuram, India

[2] Department of Mechanical Engineering, Muthayammal Engineering College, Rasipuram, India

study uses Finite Element Analysis (FEA) to analyse the stress behaviour of L4 and L5 lumber joints [9]. This method allow new design to be tested completely before manufacturing the prototype. There exist several method [10–14] to analyse the condition of affected or damaged spine and to finalise the treatment. However, no standardised FEA method combined with digital image processing is available for verification, validation of designs. Only, very few studies are reported to test the condition of other parts of body [15].

Hence, the objective of the study is to ease the process of diagnosis in the medical filed for clinicians to observe the condition of Lumbar Chronic Disc Malady (LDDD) to protect the coverings of outer tissues. This can be executed using the execution of 3D surface from the true image segmentation and mesh generation. This 3D model obtained from this state-of-art model is simulated by FEA. The study aims at the generation of 3D objects of human spine to analyse the biomechanical behaviour [16–25]. This is initially carried out through filtering to smoothen the image and segmentation using various edge detection technique. Further, the generation of 3D meshing is used to calculate the various stress factors at different loading condition and angles.

In this paper, the proposed method aims to generate a mesh model of a spine that simulates numerically the biomedical properties of two vertebrae (L4 and L5) of human spine and an inter vertebrae disc using Finite Element Analysis (FEA) technique. In the proposed system, the bony areas in MRI image is segmented using edge detection techniques and the smoother surfaces from boundary lines are obtained using filtering techniques. Further, the proposed method aims to generate high quality meshes that exploits linear characteristic for the processing of mesh for agreement.

The use of FEA is used for conducting the experiments under different bone lifting conditions and it is subjected to different loads like 490 N, 539 N, 588 N, 637 N and 686 N. Various weights (50 KG, 55 KG, 60 KG, 65 KG and 70 KG) are used to carry out the stress weights at different angles (30°, 60° and 90°). The entire analysis is carried out in lumbar bone (L4 and L5) that originates from pedicles curve. The lumbar vertebrae regions is used as potential break zones and analyzed in the form of upright posture with different loading conditions. The FEA results are matched with human lumbar spine biomechanical properties [26]. The two vertebrae (L4 and L5) of human spine is regarded as the linear materials with the exclusion of ligaments. The system analyses the behaviour of contact between the bones, disc simulation and stress and displacements on human lumbar spine. After the stress distribution calculation, the maximum von misses stress and magnitude value is estimated in the regions of L5/S1. The FEA is used to estimate the stretching limits of lumbar spine.

The outline of the paper is mentioned as follows: Section 2 provides the Filtering Human Lumbar Spine Images. Section 3 provides various edge detection technique. Section 4 discusses the Simulation on Real Dataset using FEA. Section 5 shows the experimental results and discussion. Finally, section 5 concludes the paper with future work.

Filtering human lumbar spine images

The main aim of denoising methods in image tends to degraded noises from original image, which is given by

$$v(i) = u(i) + n(i) \tag{1}$$

where.

$v(i)$ observed value,
$u(i)$ true value and
$n(i)$ pixel noise perturbation
i pixel.in an image

The proposed study uses three different filters for the purpose of testing the proposed model, which is given in following section.

Mean filter

Mean filtering is the simplest method for images smoothening. Each image pixel with windowing function output is averaged to obtain final result. This helps in removal of noises at the time of sources of noise being zero-mean and additive. The signal noise (x) in one dimensional window of length N is given by,

$$x_{noise}(_i) = X_i, \forall i \in 1 \leq n \leq N \tag{2}$$

where.

X_i - random number, where the values of $E[X]$ is considered as zero and then it applies one 1 dimensional window W_r on x_{noise} signal and this results in

$$W_r(i) = (x_{noise}(i-r), \ldots, x_{noise}(0), \ldots, x_{noise}(i+r)) \tag{3}$$

Finally the mean of one dimensional window W_r is given by,

$$mean(W_r(i)) = P_i + r_j = i-r x_{noise}(j)\ (2r+1) \tag{4}$$

With increase in the size of window r, the following condition is observed,

$$lim_{r \to \infty} mean(W_r(i)) = 0\infty = 0 \tag{5}$$

The expectation value E[X] = 0 is not required and the filtering is used to removing the entire noise present in the image.

The mean filters helps in avoiding the problem associated with removal of useful information form an image and it works well over uniform area. The information is made piecewise uniform by the use of this non-linear mean filter [27–30].

Trimmed and hybrid median filters

The median filter provides neighbourhood shape that affect significantly the filter behavior. This information is passed as in convolution over an image, however instead considering the weighted sum of neighbourhood elements, the median value is considered and the neighbourhood centered at i, j is given by N_{ij} and the filter information is thus described by

$$y_{ij} = \text{med}\left(\{x_{uv} | x_{uv} \in N_{ij}\}\right) \quad (6)$$

The median filter performs better filtering than the linear filters, since it rejects large noise values or outliers. The absence of outliers makes the median filter to perform at a poorer way. The noises with large values is called as long-tailed noise, since the probability density value of noises has longer tails and the density weight is far from mean. On the other hand, the noises without such characteristic is called as short-tailed noise [31].

The former noise produces very less number of large noise values and that does not affect the median and vice versa. This constraint is handled using trimmed linear filter with a removed of a percentage of large or small neighborhood values.

Non Local Means (NL) Filter

Non Local Means (NL) filter based on a non-local averaging of all pixels in the image. Consider a noisy discrete image $v = \{v(i) \mid i \in I\}$, and the value estimated for a pixel (i) is given by $NL[v](i)$ and this is represented as a pixels weighted average in the image,

$$NL[v](i) = \sum_{j \in I} w(i,j) v(j) \quad (7)$$

where $\{w(i,j)\}_j$ - family of weights that depend on pixel similarity, and it should satisfy a condition $0 \leq w(i,j) \leq 1$ and $\sum_j w(i,j) = 1$.

The similarity between any two pixels i and j depends mainly on similarity between gray level intensity vectors $v(N_i)$ and $v(N_j)$ and the fixed size square neighborhood is given by N_k and this is centered around a pixel k. This similarity measurement is estimated in terms of reducing function of a Euclidean distance. The NL-means filtering compares the similarity between the grey levels in a single point and further it measures the whole neighborhood geometrical configuration [12].

Edge detection for human lumbar spine images

LoG edge detection

The Laplacian of Gaussian (LoG) of an image $f(x,y)$ is represented in terms of second order derivative. The LoG operates under two different effects, the first effect is used to smoothen the given image and second effect computes the Laplacian and this helps to obtain double edge image. The edges are usually located the discovery of zero crossings between any two double edges. The Laplacian function is implemented using a mask and it is used to find the darker or lighter edge side in a pixel.

Marr-hildreth edge detection

The Marr-Hildreth edge detection method is used to detect the edges in the form of a continuous curves that has a fast variations and well-built in brightness of an image. This is a easier process and it image convolution is used along with LoG function or it can be calculated as DoG quick approximation. Further, filtered results provide zero-crossings that helps in finding the edges. This method involves smoothening image using Gaussian function and then 2D Laplacian is applied to smoothen the image further. If there exist a sign change greater than threshold level, the pixel is marked as edge. The Hysteresis is used to run the Laplacian, similar to canny edge detection [32].

Robinson edge detection

The Robinson edge method is easier to be implemented since it relies on the value of coefficients (0, 1 and 2). There are symmetrical masks around directional axis with zeros. The results of only 4 different masks are computed and other four masks result is obtained by negating first four results. The gradient magnitude is considered as a maximum one and it is obtained by the application of 8 masks to the neighborhood pixel. The approximation of gradient angle takes place in the form of zeroes line angle in the mask and that yields atmost response.

Kirsch edge detection

Kirsch edge detection uses the similar principle as Robinson edge detection method. The masks is defined by the selection of a single mask and then it is routed to eight compass directions. The magnitude of edges are defined in terms of maximum obtained edge convoluted value of each mask. The maximum magnitude obtained from a mask represents the direction [8, 33–36].

Simulation on real dataset using FEA

Generation of mesh

The FEA approximates the solution to a boundary value specifically for the differential equations, which is regarded as a numerical technique. The optimal validation is generated for the proposed model and preprocessing phase is used to perform the initial start for simulation. The simulation using FEA is used to check the performance of the proposed model. The proposed model is divided into finite surfaces using ANSYS software, it is then transformed into volumes, which helps in the formation of 3D meshes using the process of meshing. The mesh illustrates the geometrical model that helps in labelling the element and it is applied on the proposed spine model by resolving the constraints under different boundary conditions. This formation is called as grids and it distributes the points in physical region, which is used mainly for numerical application. The 3D structures helps in formation of mesh on solids and surfaces. These meshes is carried out for simulation using real medical data set spine model.

Generating mesh

The surface mesh is produced using surface triangulation in FEA and it resembles the volume mesh and geometry model. The input to it is fetched and it forms a different criterion for surface triangulation. ANSYS software develops the surface mesh and uses complex vertex post stressing of geometric model. This calculates the TriMesh method and that involves triangular elements. The 2D parametric surface representation is used to design the mesh elements and it is used to visualize the 3D shape using node localities. The shapes of generated triangular element is generated in equilateral triangular shape and the resolving process is slow. The input surface is used to experiment the triangulation point sets. The implicit equation is used to derive a smooth input surface. Finally, a surface mesh with high quality is generated using MRI scanning on a person is used widely on computer graphics, geometric modeling and finite element methods (Fig. 1).

Meshing

The FEA aims at searching the parameters of spine geometry and that utilizes the help of finite element mesh. Direct conversation method is used to attain spine meshes specific to subject. In this method, the image voxel is used to generate mesh and finally it is transformed to hexahedral structures. The segregation of image voxel separated parts takes place and it is then transformed directly into meshes with brick elements. The image densities are estimated and then it is used

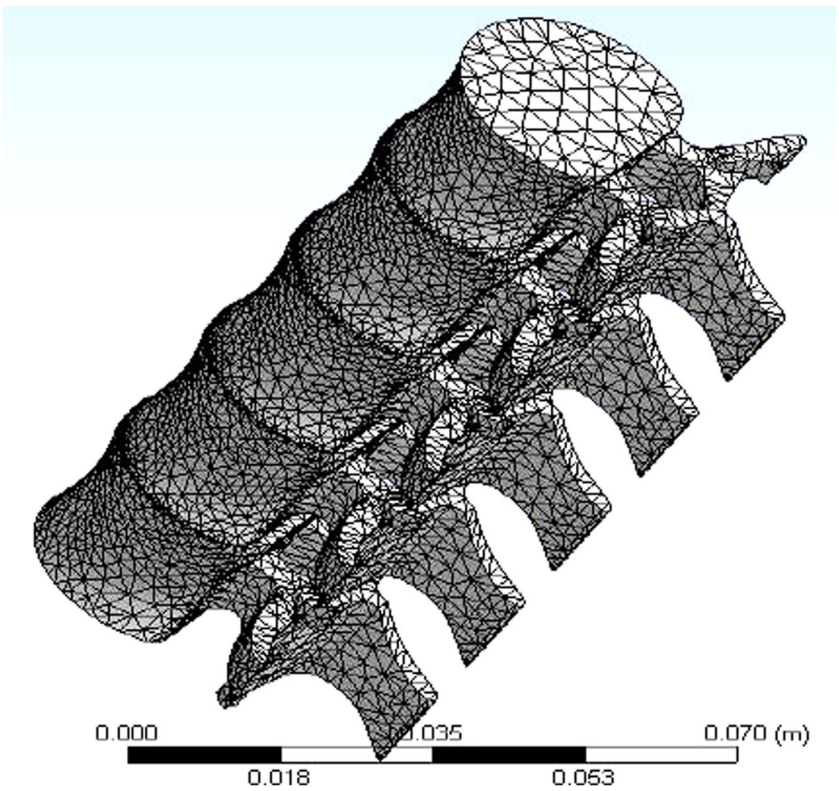

Fig. 1 Illustration of meshing on proposed spine model

Table 1 Comparison of proposed model in terms of various filters and edge detection algorithm

Sigma = 0.013 Threshold = 0.21

Edge Detection Algorithm	Parameters				
	Average Magnitude	Density of Edge Length	Initial Position	Final Threshold	Fine Tuned Image
Mean Filter					
Before Edge detection	13.24	2.0054	7.62	6.09	7.62
After Edge Detection					
LoG edge detection	16.35	0	7.67	8.52	8.61
Marr-Hildreth Edge Detection	10.75	1	6.37	5.97	6.37
Robinson Edge detection	10.70	1	6.35	5.98	6.38
Kirsch Edge detection	12.90	1	7.45	6.93	7.45
Trimmed and Hybrid Median Filters					
Before Edge Detection	32.22	1.0039	14.61	15.70	16.61
After Edge Detection					
LoG edge detection	16.35	0	8.67	8.52	8.67
Marr-Hildreth Edge Detection	10.78	1	6.36	5.95	6.34
Robinson Edge detection	10.68	1	6.30	5.04	6.34
Kirsch Edge detection	12.94	1	7.4	6.36	7.45
NL Filter					
Before Edge Detection	14.39	2.0095	8.17	7.64	8.17
After Edge Detection					
LoG edge detection	13.89	0	5.04	7.38	7.44
Marr-Hildreth Edge Detection	8.13	0	4.56	4.74	0
Robinson Edge detection	8.04	0	4.54	4.69	0
Kirsch Edge detection	9.32	1	5.68	5.28	5.66

Table 2 Results of various loading conditions at 30°

Object Name	Min/Max	Load@ 490 N	Load@ 539 N	Load @ 588 N	Load@ 637 N	Load @ 686 N
TD	Min	0. m	0. m	0. m	0. m	0. m
	Max	2.8635e - 004 m	3.1499e-004 m	3.4362e-004 m	3.7226e-004 m	4.0089e-004 m
EES	Min	2.6252e-011 m/m	3.9144e-011 m/m	4.2267e-011 m/m	3.1499e-011 m/m	4.9905e-011 m/m
	Max	3.7783e-003 m/m	4.1561e-003 m/m	4.5339e-003 m/m	4.9117e-003 m/m	5.2896e-003 m/m
MAX PES	Min	−5.9301e-007 m/m	−6.5232e-007 m/m	−7.1162e-007 m/m	−7.7092e-007 m/m	−8.3022e-007 m/m
	Max	3.6966e-003 m/m	4.0662e-003 m/m	4.4359e-003 m/m	4.8055e-003 m/m	5.1752e-003 m/m
MIN PES	Min	−1.0744e-003 m/m	−1.1819e-003 m/m	−1.2893e-003 m/m	−1.3968e-003 m/m	−1.5042e-003 m/m
	Max	3.8894e-008 m/m	4.2784e-008 m/m	4.6673e-008 m/m	5.0563e-008 m/m	5.4452e-008 m/m
NES	Min	−7.6042e-004 m/m	−8.3646e-004 m/m	−9.125e-004 m/m	−9.8855e-004 m/m	−1.0646e-003 m/m
	Max	3.059e-004 m/m	3.3649e-004 m/m	3.6708e-004 m/m	3.9767e-004 m/m	4.2826e-004 m/m
SES	Min	−7.1699e-004 m/m	−7.8869e-004 m/m	−8.6039e-004 m/m	−9.3209e-004 m/m	−1.0038e-003 m/m
	Max	7.3844e-004 m/m	8.1228e-004 m/m	8.8612e-004 m/m	9.5997e-004 m/m	1.0338e-003 m/m
ES	Min	0.14971 Pa	0.24724 Pa	0.28234 Pa	0.17181 Pa	0.30225 Pa
	Max	5.9289e+007 Pa	6.5218e+007 Pa	7.1147e+007 Pa	7.7076e+007 Pa	8.3005e+007 Pa
MAX PS	Min	−2.9126e+006 Pa	−3.2039e+006 Pa	−3.4951e+006 Pa	−3.7864e+006 Pa	−4.0776e+006 Pa
	Max	6.3059e+007 Pa	6.9364e+007 Pa	7.567e+007 Pa	8.1976e+007 Pa	8.8282e+007 Pa
MIN PS	Min	−1.8094e+007 Pa	−1.9904e +007 Pa	−2.1713e+007 Pa	−2.3523e+007 Pa	−2.5332e+007 Pa
	Max	7.3053e+006 Pa	8.0358e +006 Pa	8.7664e+006 Pa	9.4969e+006 Pa	1.0227e+007 Pa
NS	Min	−1.2017e+007 Pa	−1.3219e+007 Pa	−1.442e+007 Pa	−1.5622e+007 Pa	−1.6824e+007 Pa
	Max	1.0009e+007 Pa	1.101e +007 Pa	1.2011e+007 Pa	1.3012e+007 Pa	1.4013e+007 Pa
SS	Min	−4.6174e+006 Pa	−5.0792e +006 Pa	−5.5409e+006 Pa	−6.0026e+006 Pa	−6.4644e+006 Pa
	Max	4.7555e+006 Pa	5.2311e +006 Pa	5.7066e+006 Pa	6.1822e+006 Pa	6.6578e+006 Pa

Table 3 Results of various loading conditions at 60°

Object Name	Min/Max	Load@ 490 N	Load @ 539 N	Load @ 588 N	Load @ 637 N	Load@ 686 N
TD	Min	0. m	0. m	0. m	0. m	0. m
	Max	4.9329e-004 m	5.4261e-004 m	5.9194e-004 m	6.4127e-004 m	6.906e-004 m
EES	Min	3.2408e-011 m/m	5.557e-011 m/m	6.1105e- 011 m/m	6.5586e-011 m/m	7.0813e-011 m/m
	Max	6.748e-003 m/m	7.4228e-003 m/m	8.0976e-003 m/m	8.7724e-003 m/m	9.4472e-003 m/m
MAX PES	Min	−2.6628e-006 m/m	−2.9291e-006 m/m	−3.1954e-006 m/m	−3.4616e-006 m/m	−3.7279e-006 m/m
	Max	6.601e-003 m/m	7.2611e-003 m/m	7.9212e-003 m/m	8.5813e-003 m/m	9.2414e-003 m/m
MIN PES	Min	−1.9219e-003 m/m	−2.1141e-003 m/m	−2.3063e-003 m/m	−2.4985e-003 m/m	−2.6907e-003 m/m
	Max	2.5388e-006 m/m	2.7927e-006 m/m	3.0466e-006 m/m	3.3005e-006 m/m	3.5544e-006 m/m
NES	Min	−1.3307e-003 m/m	−1.4637e-003 m/m	−1.5968e-003 m/m	−1.7299e-003 m/m	−1.8629e-003 m/m
	Max	5.4133e-004 m/m	5.9547e-004 m/m	6.496e-004 m/m	7.0373e-004 m/m	7.5787e-004 m/m
SES	Min	−1.2654e-003 m/m	−1.3919e-003 m/m	−1.5185e-003 m/m	−1.645e-003 m/m	−1.7715e-003 m/m
	Max	1.3102e-003 m/m	1.4412e-003 m/m	1.5722e-003 m/m	1.7032e-003 m/m	1.8342e-003 m/m
ES	Min	0.32528 Pa	0.49064 Pa	0.48578 Pa	0.30407 Pa	0.31183 Pa
	Max	1.0521e+008 Pa	1.1574e+008 Pa	1.2626e+008 Pa	1.3678e+008 Pa	1.473e+008 Pa
MAX PS	Min	−5.0613e+006 Pa	−5.5675e+006 Pa	−6.0736e+006 Pa	−6.5798e+006 Pa	−7.0859e+006 Pa
	Max	1.1258e+008 Pa	1.2384e+008 Pa	1.351e+008 Pa	1.4636e+008 Pa	1.5762e+008 Pa
MIN PS	Min	−3.2397e+007 Pa	−3.5637e+007 Pa	−3.8877e+007 Pa	−4.2116e+007 Pa	−4.5356e + 007 Pa
	Max	1.309e+007 Pa	1.4399e+007 Pa	1.5708e+007 Pa	1.7017e+007 Pa	1.8326e+007 Pa
NS	Min	−2.1164e+007 Pa	−2.328e+007 Pa	- 2.5396e+007 Pa	−2.7513e+007 Pa	−2.9629e + 007 Pa
	Max	1.7765e+007 Pa	1.9541e+007 Pa	2.1317e+007 Pa	2.3094e+007 Pa	2.487e + 007 Pa
SS	Min	−8.1491e+006 Pa	−8.964e+006 Pa	−9.7789e+006 Pa	−1.0594e+007 Pa	−1.1409e + 007 Pa
	Max	8.4375e+006 Pa	9.2812e+006 Pa	1.0125e+007 Pa	1.0969e+007 Pa	1.1812e+007 Pa

Table 4 Results of various loading conditions at 90°

Object Name	Min/ Max	Load@490 N	Load@539 N	Load@ 588 N	Load@637 N	Load@686 N
TD	Min	0. m	0. m	0. m	0. m	0. m
	Max	8.0061e-006 m	8.8067e-006 m	9.6073e-006 m	1.0408e-005 m	1.1209e-005 m
EES	Min	1.7201e-012 m/m	1.6773e-012 m/m	1.7311e-012 m/m	2.004e-012 m/m	2.0299e-012 m/m
	Max	2.1051e-004 m/m	2.3156e-004 m/m	2.5261e-004 m/m	2.7366e-004 m/m	2.9471e-004 m/m
MAX PES	Min	−7.4681e-008 m/m	−8.2149e-008 m/m	−8.9617e-008 m/m	−9.7086e-008 m/m	−1.0455e-007 m/m
	Max	5.8237e-005 m/m	6.4061e-005 m/m	6.9885e-005 m/m	7.5709e-005 m/m	8.1532e-005 m/m
MIN PES	Min	−2.0881e-004 m/m	−2.2969e-004 m/m	−2.5057e-004 m/m	−2.7145e-004 m/m	−2.9233e-004 m/m
	Max	1.4084e-007 m/m	1.5492e-007 m/m	1.6901e-007 m/m	1.8309e-007 m/m	1.9718e-007 m/m
NES	Min	−1.5177e-005 m/m	−1.6695e-005 m/m	−1.8213e-005 m/m	−1.973e-005 m/m	−2.1248e-005 m/m
	Max	4.1301e-005 m/m	4.5431e −005 m/m	4.9561e-005 m/m	5.3691e-005 m/m	5.7821e-005 m/m
SES	Min	−4.3206e-005 m/m	−4.7527e-005 m/m	−5.1847e-005 m/m	−5.6168e-005 m/m	−6.0488e-005 m/m
	Max	3.7105e-005 m/m	4.0816e-005 m/m	4.4526e-005 m/m	4.8237e-005 m/m	5.1947e-005 m/m
ES	Min	8.5377e-003 Pa	8.3173e-003 Pa	7.25e-003 Pa	1.194e-002 Pa	8.1018e-003 Pa
	Max	3.3655e+006 Pa	3.702e+006 Pa	4.0386e+006 Pa	4.3751e+006 Pa	4.7117e+006 Pa
MAX PS	Min	−5.7897e +005 Pa	−6.3687e+005pa	−6.9477e+005pa	−7.5266e+005 pa	−8.1056e+005pa
	Max	9.9558e+005 Pa	1.0951e+006pa	1.1947e+006pa	1.2943e+006 pa	1.3938e+006
MIN PS	Min	−3.3585e+006 Pa	−3.6944e+006 Pa	−4.0302e+006 Pa	−4.3661e+006 Pa	−4.7019e+006 Pa
	Max	88,841 Pa	97,726 Pa	1.0661e+005 Pa	1.1549e+005 Pa	1.2438e+005 Pa
NS	Min	−6.9212e+005 Pa	−7.6133e+005 Pa	−8.3054e+005 Pa	−8.9975e+005 Pa	−9.6897e+005 Pa
	Max	6.3143e+005 Pa	6.9457e+005 Pa	7.5771e+005 Pa	8.2085e+005 Pa	8.84e+005 Pa
SS	Min	−2.7825e +005 Pa	−3.0607e+005pa	−3.339e+005 pa	−3.6172e+005 pa	−3.8955e+005 pa
	Max	2.3896 + e005 Pa	2.6285e+005pa	2.8675e+05 pa	3.1064e+005pa	3.3454e+005 pa

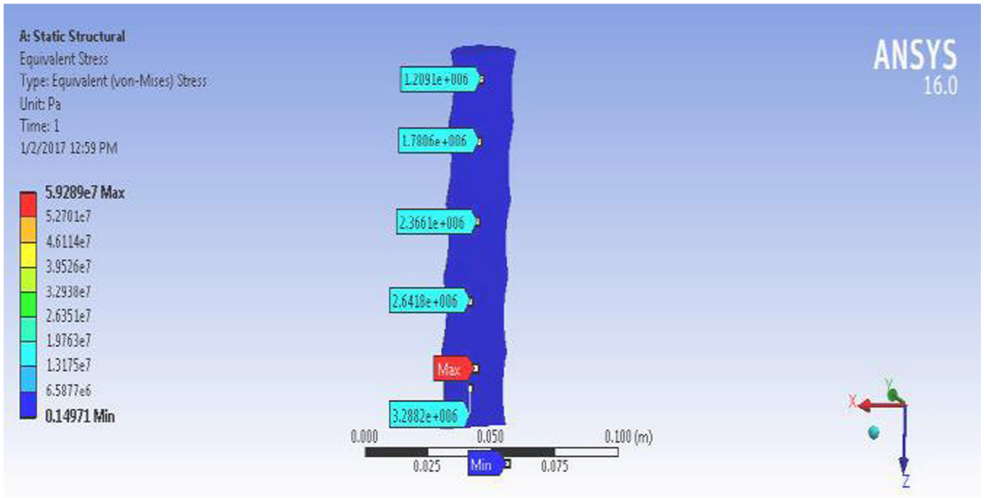

Fig. 2 Result of spine under loading of 50 kg at 60°

for defining the behavior of the material. In specific, the behavior of the material is found using element-by-element approach.

Here, the spine image intensity is directly related with the values of image density and finally the values of Young's modulus is obtained. The modulus values are computed using a numerical process but the accurate behavior at the time of vertebrae tissues generation is considered as a challenging task. The Tetrahedron method with fine components helps in achieving the process of meshing and then the entire spine region is embed into a smaller triangular shape.

Results and discussion

This section is used to estimate the efficiency of proposed method. The proposed method uses Hausdorff distance and error probability method in segmenting an image using proposed boundary detection method.

The proposed method is compared in terms of several edge detection methods from various filters. The Table 1 presents different metrics like edge length density, average magnitude, final threshold, initial position, and fine-tuned image obtained from image segmentation process. These results are collected and noted for various filters like Mean Filter, Trimmed and Hybrid Median Filters and NL Filter. Also, the method is compared with other edge detection methods like LoG edge detection, Marr-Hildreth Edge Detection, Robinson Edge detection and Kirsch Edge detection.

Load displacement

The load displacement on L1 surface is estimated using certain measurements that include: 490 N, 539 N, 588 N, 637 N, and 686 N, where the angle of estimation is varied in terms of 30°, 60° and 90° and the results are given in Tables 2, 3 and 4, respectively. It is seen from the results that L1 surface has the ability to tolerate a 686 N load (that represents a 70 kg healthy

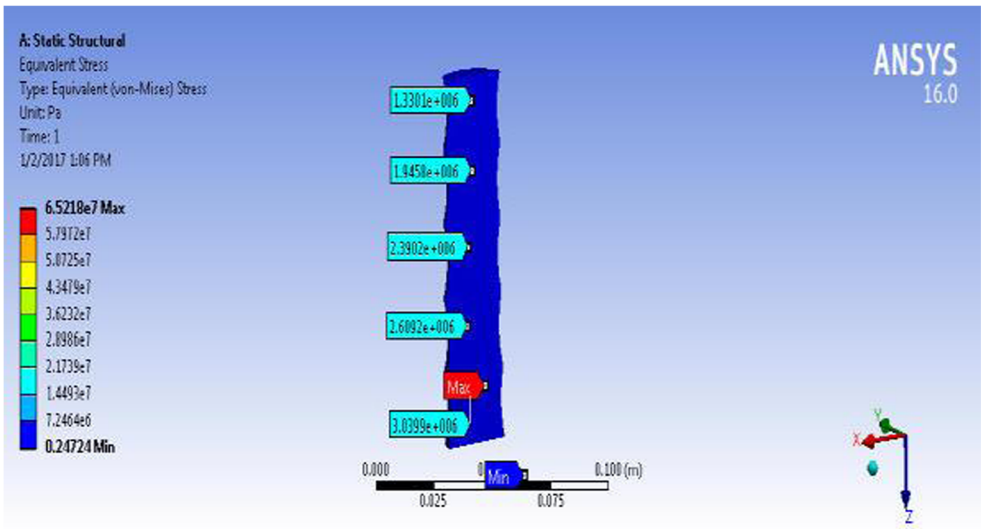

Fig. 3 Result of spine under loading of 55 kg at 60°

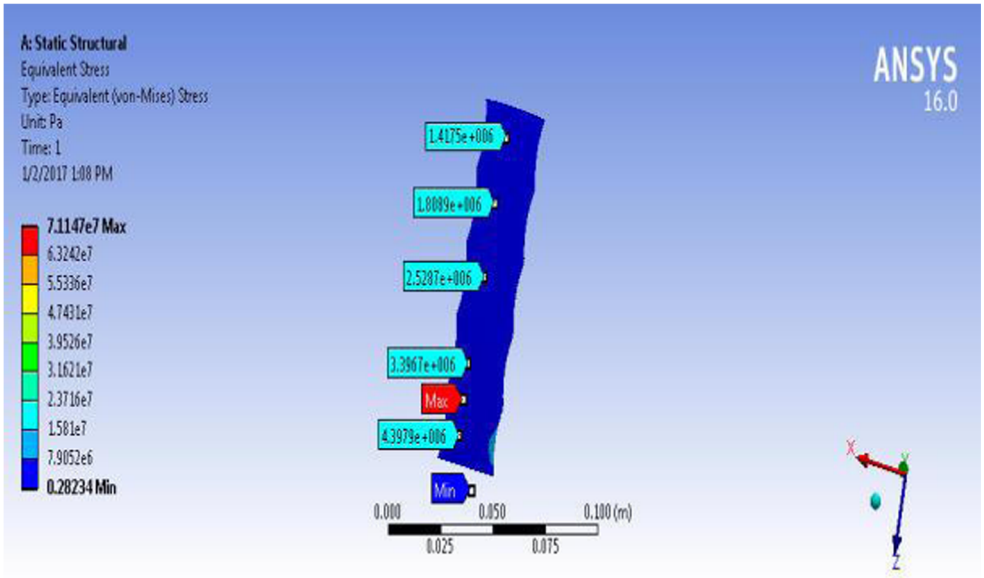

Fig. 4 Result of spine under loading of 60 kg at 60°

person who stands straight in a relaxed state). The level of tolerance is increased up to 2500 N, when a person lifts load in his two arms in a straight position. It is further noted that the L1 surface tolerates more as the load lifts becomes heavier. At the time of heavy load, the L1 surface tolerates with load displacement behavior at the time of axial compression. The withstanding tolerance level on the proposed model shows the biomechanical physiognomies on flexible vertebral bone. Further, the results of different loads on various angles are given in Figs. 1, 2, 3, 4, 5 and 6.

The result further shows an injury on a patient w.r.t bone displacements, which is formed at the stage of L4 spinous process. Further, the lamina bone stress is identified at facet joint of L4 and L5. The post-operation result of the proposed model geometry defines the distance between the two spinous points has similar measurements obtained from both the geometries. Here, the spine bone load is directly proportional to the stress concentration in pedicle region. L1 vertebral bone displacement is initiated by vertebral body compression and superior articular compression in downward direction. The vertebra movement at the time of restraints and applied load on the proposed model helps in the creation of high stress in spine pedicle region. The outcomes of lumbar spine analysis is shown in preceding diagrams under different weight conditions like 50 - 70 kg that increases at a rate of 5 kg at different angles, say, 30°, 60° and 90°.

The parameters of stress distribution on a proposed spine model at different loading conditions and angles is shown in Table 5. The result shows that spine pedicel region acts with high stress due to applied loading condition. The spine

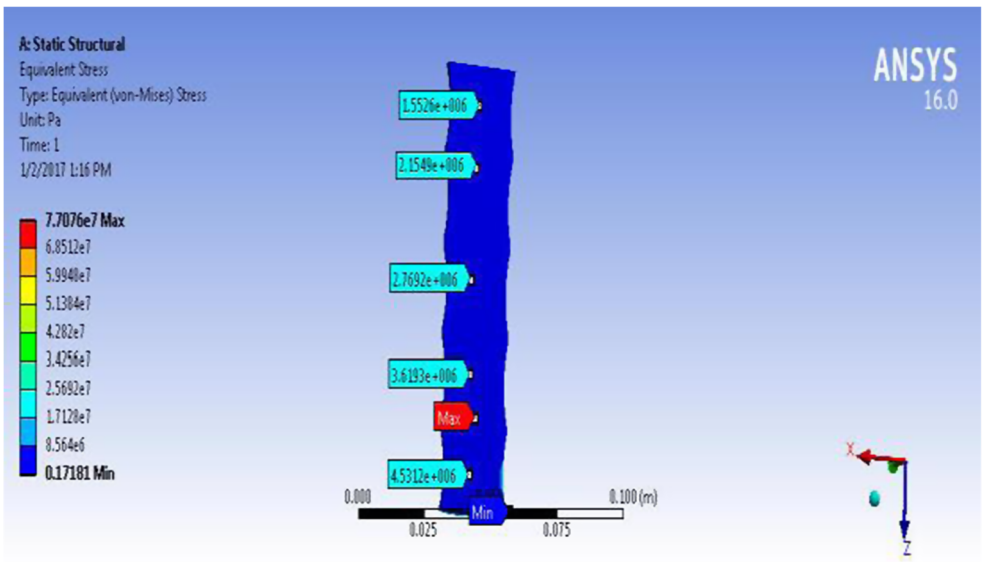

Fig. 5 Result of spine under loading of 65 kg at 60°

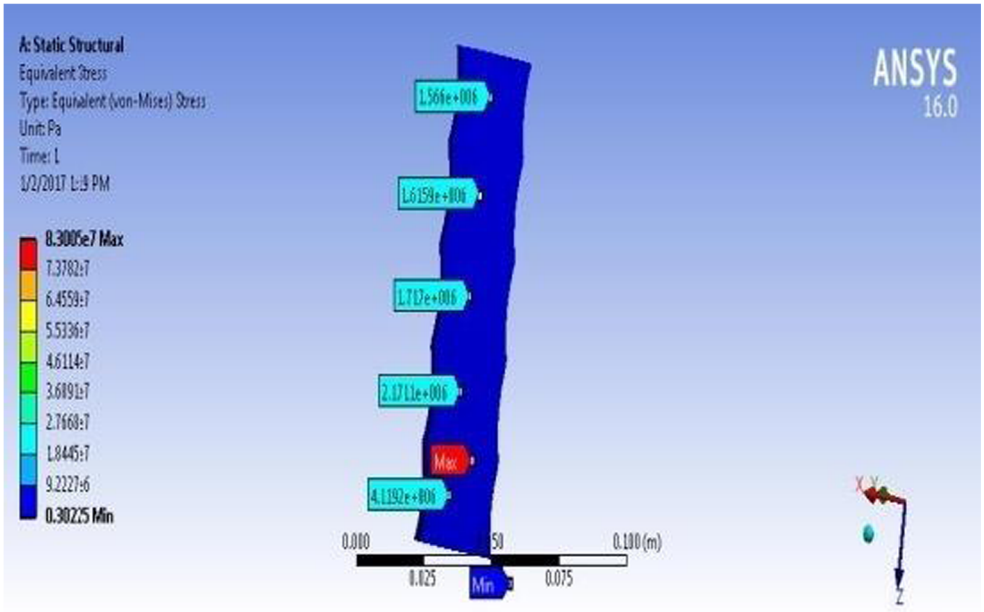

Fig. 6 Result of spine under loading of 70 kg at 60°

vertebral bone on upper body is affected to a certain extent and it has higher Von-Misses stress values, which is calculated from the results as shown in Table 5.

Conclusion and future enhancement

In this paper, the proposed system analyses the biomechanics and structure of human lumbar spine MRI image under different loading conditions. This involves three different phases: preprocessing, conversion from 1D to 3D conversion and testing of stress. The image processing involves two steps: noise smothering using filters and image segmentation using edge detection techniques. The former performs the operation of removing unwanted noises in MRI spine image and latter detects the edges. The pre-processed operation is carried out using MATLAB. The result shows that median filter obtains improved performance than other algorithms. The result from these pre-processed output is sent for 3D conversion using FEA using ANSYS. The third phase involves the spine image testing under different angles and loading conditions. The use of FEA is used for conducting the experiments under different bone lifting conditions and it is subjected to different loads. Various weights are used to carry out the stress weights at different angles. The entire analysis is carried out in lumbar bone (L4 and L5) that originates from pedicles curve. The

Table 5 Stress distribution result with different loads and angles

S. No	Weight	Load(N)	Angle at	Total Deformation (mm)	Equivalent (von-Misses) Stress(MPa)	Equivalent Elastic Strain
1	50	490	30	2.8635e-004 m	5.9289e+007 Pa	3.7783e-003 m/m
	55	539		3.1499e-004 m	6.5218e+007 Pa	4.1561e-003 m/m
	60	588		3.4362e-004 m	7.1147e+007 Pa	4.5339e-003 m/m
	65	637		3.7226e-004 m	7.7076e+007 Pa	4.9117e-003 m/m
	70	686		4.0089e-004 m	8.3005e+007 Pa	5.2896e-003 m/m
2	50	490	60	4.9329e-004 m	1.0521e+008 Pa	6.748e-003 m/m
	55	539		5.4261e-004 m	1.1574e+008 Pa	7.4228e-003 m/m
	60	588		5.9194e-004 m	1.2626e+008 Pa	8.0976e-003 m/m
	65	637		6.4127e-004 m	1.3678e+008 Pa	8.7724e-003 m/m
	70	686		6.906e-004 m	1.473e+008 Pa	9.4472e-003 m/m
3	50	490	90	8.0061e-006 m	3.3655e+006 Pa	2.1051e-004 m/m
	55	539		8.8067e-006 m	3.702e+006 Pa	2.3156e-004 m/m
	60	588		9.6073e-006 m	4.0386e+006 Pa	2.5261e-004 m/m
	65	637		1.0408e-005 m	4.3751e+006 Pa	2.7366e-004 m/m
	70	686		1.1209e-005 m	4.7117e+006 Pa	2.9471e-004 m/m

lumbar vertebrae regions is used as potential break zones and analyzed in the form of upright posture with different loading conditions. The FEA results are matched with human lumbar spine biomechanical properties. The stress analysis outcomes in spine lumbar vertebra under different external loads leads to severe consequences when the frequency of excitation from external load matches with natural frequency of the spine lumbar vertebra bone. The result shows that the disc bone has the ability to withstand the load between 500 to 2500 N. The damage over nucleus pulpous takes place, when the load increases above the threshold level. The outcomes provides a better understanding of spine bone biomechanical behaviors. In future, the same model can be applied over other parts of body to check its biomechanical behavior.

Compliance with ethical standards

Conflict of interests The authors declare that this article content has no conflict of interest.

Ethical approval This article does not contain any studies with human participants or animals performed by any of the author.

Publisher's Note Springer Nature remains neutral with regard to jurisdictional claims in published maps and institutional affiliations.

References

1. Ghosh, S., Raja'S, A., Chaudhary, V., & Dhillon, G. (2011). Automatic lumbar vertebra segmentation from clinical CT for wedge compression fracture diagnosis. In Medical Imaging 2011: Computer-Aided Diagnosis (Vol. 7963, p. 796303). International Society for Optics and Photonics.
2. Schoenfeld, A. J., Bono, C. M., McGuire, K. J., Warholic, N., and Harris, M. B., Computed tomography alone versus computed tomography and magnetic resonance imaging in the identification of occult injuries to the cervical spine: A meta-analysis. *Journal of Trauma and Acute Care Surgery* 68(1):109–114, 2010.
3. Smyth, P. P., Taylor, C. J., and Adams, J. E., Automatic measurement of vertebral shape using active shape models. *Image and Vision Computing* 15(8):575–581, 1997.
4. Parthasarathy, P., & Vivekanandan, S. (2018). A numerical modelling of an amperometric-enzymatic based uric acid biosensor for GOUT arthritis diseases. *Informatics in Medicine Unlocked*.
5. Mastmeyer, A., Engelke, K., Fuchs, C., and Kalender, W. A., A hierarchical 3D segmentation method and the definition of vertebral body coordinate systems for QCT of the lumbar spine. Medical image analysis 10(4):560–577, 2006.
6. Michopoulou, S. K., Costaridou, L., Panagiotopoulos, E., Speller, R., Panayiotakis, G., and Todd-Pokropek, A., *Atlas-based segmentation of degenerated lumbar intervertebral discs from MR images of the spine*. IEEE transactions on Biomedical Engineering 56(9): 2225–2231, 2009.
7. Sundarasekar, R., Thanjaivadivel, M., Manogaran, G., Kumar, P. M., Varatharajan, R., Chilamkurti, N., and Hsu, C. H., Internet of things with maximal overlap discrete wavelet transform for remote health monitoring of abnormal ECG signals. *Journal of medical systems* 42(11):228, 2018.
8. Kumar, P. M., Lokesh, S., Varatharajan, R., Babu, G. C., and Parthasarathy, P., Cloud and IoT based disease prediction and diagnosis system for healthcare using fuzzy neural classifier. *Future Generation Computer Systems* 86:527–534, 2018.
9. Kumar, P. M., Devi, U., Manogaran, G., Sundarasekar, R., Chilamkurti, N., and Varatharajan, R., Ant colony optimization algorithm with internet of vehicles for intelligent traffic control system. *Computer Networks* 144:154–162, 2018.
10. Vijayakumar, V., Priyan, M. K., Ushadevi, G., Varatharajan, R., Manogaran, G., & Tarare, P. V. (2018). E-Health Cloud Security Using Timing Enabled Proxy Re-Encryption. *Mobile Networks and Applications*, 1–12.
11. Parthasarathy, P., and Vivekanandan, S., Investigation on uric acid biosensor model for enzyme layer thickness for the application of arthritis disease diagnosis. *Health information science and systems* 6:1–6, 2018.
12. Mathan, K., Kumar, P. M., Panchatcharam, P., Manogaran, G., & Varadharajan, R. (2018). A novel Gini index decision tree data mining method with neural network classifiers for prediction of heart disease. *Design Automation for Embedded Systems*, 1–18.
13. Priya, S., Varatharajan, R., Manogaran, G., Sundarasekar, R., & Kumar, P. M. (2018). Paillier homomorphic cryptosystem with poker shuffling transformation based water marking method for the secured transmission of digital medical images. *Personal and Ubiquitous Computing*, 1–11.
14. Varatharajan, R., Preethi, A. P., Manogaran, G., Kumar, P. M., & Sundarasekar, R. (2018). Stealthy attack detection in multi-channel multi-radio wireless networks. *Multimedia Tools and Applications*, 1–24.
15. Manogaran, G., Shakeel, P. M., Hassanein, A. S., Priyan, M. K., & Gokulnath, C. (2018). Machine-Learning Approach Based Gamma Distribution for Brian Abnormalities Detection and Data Sample Imbalance Analysis. *IEEE Access*.
16. Biswas, S., and Hazra, R., Robust edge detection based on modified Moore-neighbor. *Optik* 168:931–943, 2018.
17. Hua, Z., and Zhou, Y., Design of image cipher using block-based scrambling and image filtering. *Information Sciences* 396:97–113, 2017.
18. Roberts, M. G., Cootes, T. F., Pacheco, E., Oh, T., and Adams, J. E., Segmentation of lumbar vertebrae using part-based graphs and active appearance models. In: *International conference on medical image computing and computer-assisted intervention*. Berlin: Springer, 2009, 1017–1024.
19. Parthasarathy, P., and Vivekanandan, S., Urate crystal deposition, prevention and various diagnosis techniques of GOUT arthritis disease: A comprehensive review. *Health information science and systems* 6(1):19, 2018.
20. Raja'S, A., Corso, J. J., and Chaudhary, V., Labeling of lumbar discs using both pixel-and object-level features with a two-level probabilistic model. *IEEE transactions on medical imaging* 30(1):1–10, 2011.
21. Parthasarathy, P. (2018). Synthesis and UV detection characteristics of TiO2 thin film prepared through sol gel route. In *IOP Conference Series: Materials Science and Engineering* (Vol. 360, No. 1, p. 012056). IOP Publishing.
22. Basha, A. A., Vivekanandan, S., and Parthasarathy, P., Evolution of blood pressure control identification in lieu of post-surgery diabetic patients: A review. *Health information science and systems* 6(1):17, 2018.
23. Varadharajan, R., Priyan, M. K., Panchatcharam, P., Vivekanandan, S., and Gunasekaran, M., A new approach for prediction of lung carcinoma using back propogation neural network with decision tree classifiers. *Journal of Ambient Intelligence and Humanized Computing*:1–12, 2018.
24. Corso, J. J., Raja'S, A., & Chaudhary, V. (2008). Lumbar disc localization and labeling with a probabilistic model on both pixel and object features. In International Conference on Medical Image

Computing and Computer-Assisted Intervention (pp. 202–210). Springer, Berlin, Heidelberg.

25. Zhan, Y., Maneesh, D., Harder, M., and Zhou, X. S., Robust MR spine detection using hierarchical learning and local articulated model. In: *International conference on medical image computing and computer-assisted intervention*. Berlin: Springer, 2012, 141–148.
26. Parthasarathy, P., & Vivekanandan, S. (2018). A typical IoT architecture-based regular monitoring of arthritis disease using time wrapping algorithm. *International Journal of Computers and Applications*, 1–11.
27. Parthasarathy, P., and Vivekanandan, S., A comprehensive review on thin film-based nano-biosensor for uric acid determination: Arthritis diagnosis. *World Review of Science, Technology and Sustainable Development* 14(1):52–71, 2018.
28. Štern, D., Likar, B., Pernuš, F., and Vrtovec, T., Automated detection of spinal centrelines, vertebral bodies and intervertebral discs in CT and MR images of lumbar spine. *Physics in Medicine & Biology* 55(1):247, 2009.
29. Huang, S. H., Chu, Y. H., Lai, S. H., and Novak, C. L., Learning-based vertebra detection and iterative normalized-cut segmentation for spinal MRI. *IEEE transactions on medical imaging* 28(10): 1595–1605, 2009.
30. Wang, Z., Zhen, X., Tay, K., Osman, S., Romano, W., and Li, S., Regression segmentation for $ M^{3} $ spinal images. *IEEE transactions on medical imaging* 34(8):1640–1648, 2015.
31. Goel, V. K., and Nyman, E., Computational modeling and finite element analysis. Spine 41:S6–S7, 2016.
32. Lujan, A. E., Balter, J. M., and Ten Haken, R. K., A method for incorporating organ motion due to breathing into 3D dose calculations in the liver: Sensitivity to variations in motion. *Medical physics* 30(10):2643–2649, 2003.
33. Eom, J., Xu, X. G., De, S., and Shi, C., Predictive modeling of lung motion over the entire respiratory cycle using measured pressure-volume data, 4DCT images, and finite-element analysis. *Medical physics* 37(8):4389–4400, 2010.
34. Gustafson, H. M., Cripton, P. A., Ferguson, S. J., and Helgason, B., Comparison of specimen-specific vertebral body finite element models with experimental digital image correlation measurements. *Journal of the mechanical behavior of biomedical materials* 65: 801–807, 2017.
35. Wang, G., Liu, Y., Xiong, W., and Li, Y., An improved non-local means filter for color image denoising. *Optik* 173:157–173, 2018.
36. Lokesh, S., Kumar, P. M., Devi, M. R., Parthasarathy, P., and Gokulnath, C., An automatic tamil speech recognition system by using bidirectional recurrent neural network with self-organizing map. *Neural Computing and Applications*:1–11, 2018.